ADVANCED MATERIALS

Supporting Information

Cation-Disorder Engineering Promotes Efficient Charge-Carrier Transport in AgBiS$_2$ Nanocrystal Films

Marcello Righetto, Yongjie Wang, Karim A. Elmestekawy, Chelsea Q. Xia, Michael B. Johnston, Gerasimos Konstantatos and Laura M. Herz*

Cation-Disorder Engineering Promotes

Efficient Charge-Carrier Transport in AgBiS₂ Nanocrystal Films

Marcello Righetto[1], Yongjie Wang[2], Karim A. Elmestekawy[1], Chelsea Q. Xia[1],

Michael B. Johnston[1], Gerasimos Konstantatos[2,3]*, Laura M. Herz[1,4]*

[1.] Department of Physics, University of Oxford, Clarendon Laboratory, Parks Road, Oxford, OX1 3PU, United Kingdom

[2.] ICFO—Institut de Ciencies Fotoniques, The Barcelona Institute of Science and Technology, Castelldefels, Barcelona, Spain

[3.] ICREA-Institució Catalana de Recerca i Estudia Avançats, Lluis Companys 23, 08010 Barcelona, Spain

[4.] Institute for Advanced Study, Technical University of Munich, Lichtenbergstrasse 2a, D-85748 Garching, Germany

*Corresponding Author's Email: laura.herz@physics.ox.ac.uk

Materials & Methods

Nanocrystals Synthesis and Thin Film Preparation

$AgBiS_2$ nanocrystals (NCs) are synthesized following previous report with Schlenk line technique [1,2]. Briefly, 4 mmol bismuth acetate, 3.2 mmol silver acetate, 24 mL oleic acid and 15 mL1-octadecene were loaded into a three-neck flask and pumped at 100°C for 2 hours to remove oxygen and moisture. The flask was then filled with argon and 4 mmol hexamethyldisilathiane with 5 mL pre-dried 1-octadecene was swiftly injected into the flask. The heating mantel was removed after ~1 min and the flask was cooled down with water bath. The nanocrystals were precipitated by adding acetone as antisolvent, followed by centrifugation at 4000 rpm for 5min. The nanocrystals were further re-dispersed into toluene and precipitated with acetone two more times. Finally, the nanocrystals were dissolved into anhydrous toluene with a concentration of 20 $mg·mL^{-1}$ and kept in ambient atmosphere for further use.

The $AgBiS_2$ nanocrystal films were prepared on z-cut quartz substrates. The substrates were soaked in 1% v/v 3-mercaptopropionic acid (MPA)/methanol solution to improve the adhesion of $AgBiS_2$ nanocrystals. The layer-by-layer deposition procedure followed previous report [2]. For each $AgBiS_2$ nanocrystal layer, one drop of 20 $mg·mL^{-1}$ nanocrystal solution was applied on the substrate during spinning at 2000 rpm. The substrate spinning was then stopped and 3-MPA/methanol 1% v/v solution was applied to fully cover the nanocrystal film for ligand-exchange. After 45 seconds, the ligand solution was span off the substrate, followed with methanol rinse twice and once with toluene. 8 layers (~80 nm) were built to achieve a decent thickness for optical measurements. The films were further transferred into glovebox for annealing at different temperatures for 10 min.

Morphology of AgBiS$_2$ NC Thin Films and Cation-Disorder Characterisation

For a complete structural characterization of the AgBiS$_2$ NC thin films studied here, we refer the reader to the work by Wang et al.[2]. Briefly, transmission electron microscopy (TEM) revealed a NC size of 6.2±0.8 nm remaining constant after the annealing at 115°C, while some necking was observed at 150°C and became predominant at higher annealing temperatures (not explored in this present study). On the other hand, X-ray diffraction (XRD) showed a significant sharpening of the peaks upon thermal annealing (Figure S8 of the reference). By combining TEM measurements and first-principle simulations, such evolution of the XRD spectra with temperature was demonstrated to originate from a rearrangement in the cation distribution within the nanocrystals, thus indicating an increasingly homogeneous cation disorder at higher annealing temperatures (Figure S11 of the reference). Such rearrangements of the cation distribution were further confirmed by high-resolution TEM measurements, indicating a change in the average Ag-S bond length (Figure S12 of the reference). AgBiS$_2$ NC thin films used in this study were further characterised by XRD to confirm the cation homogeneization. XRD data were collected using a Rigaku SmartLab powder diffractometer in the Bragg–Brentano geometry with Cu Kα radiation. The measured XRD patterns for the set of samples used in this work (Figure S2) perfectly reproduce the findings reported by Wang et al. [2].

 Absorption Measurements

Visible-NIR absorption spectra were measured using a Bruker-Vertex 80v Fourier-Transform Infrared (FTIR) spectrometer fitted with a transmission/reflection accessory. Spectra in the region 0.5 – 1.22 eV were taken by using a tungsten halogen source and an InSb detector, and spectra in the region 1.22 – 2.5 eV were taken by using a tungsten halogen source and a Si detector. The two datasets obtained were stitched by matching the absorbance curves at 1.22eV. For low-temperature

measurements, the samples were mounted in a gas-exchange helium cryostat (OptistatCF2, Oxford Instruments) under a helium atmosphere. The temperature was varied between 30 K and 295 K in either 5 K or 10 K increments.

Optical-Pump-Terahertz-Probe Spectroscopy

For optical pump terahertz probe (OPTP) measurements, we used a setup that has been described in detail previously [3]. Briefly, 1.55 eV emission with 35-fs pulse duration and 5-kHz repetition rate is provided by an amplified Ti:sapphire laser system (Spectra-Physics Spitfire). This fundamental output was used to generate single-cycle THz radiation pulses in a spintronic emitter via the inverse spin Hall effect [4]. In our setup, the THz and pump beams are incident on the thin film sample in collinear geometry. Fractional changes in the THz transmission are measured by using free-space electro-optic (EO) sampling. The THz detection setup comprises a 1 mm-thick ZnTe (110) crystal, a Wollaston prism and a pair of balanced photodiodes. In the setup, samples are excited by frequency-doubled 3.1-eV pulses, obtained by second-harmonic generation in a beta-barium-borate (BBO) crystal. We measured $AgBiS_2$ NC thin-film samples deposited onto 2-mm thick z-cut quartz. During OPTP measurements, the THz emission and detection setups, and samples are kept under vacuum at pressures below 0.1 mbar. For the temperature-dependent measurements, samples were mounted in a cold-finger cryostat (MicrostatHe, Oxford Instruments) and cooled by liquid helium. The temperature was regulated via a temperature controller connected to a resistive heater.
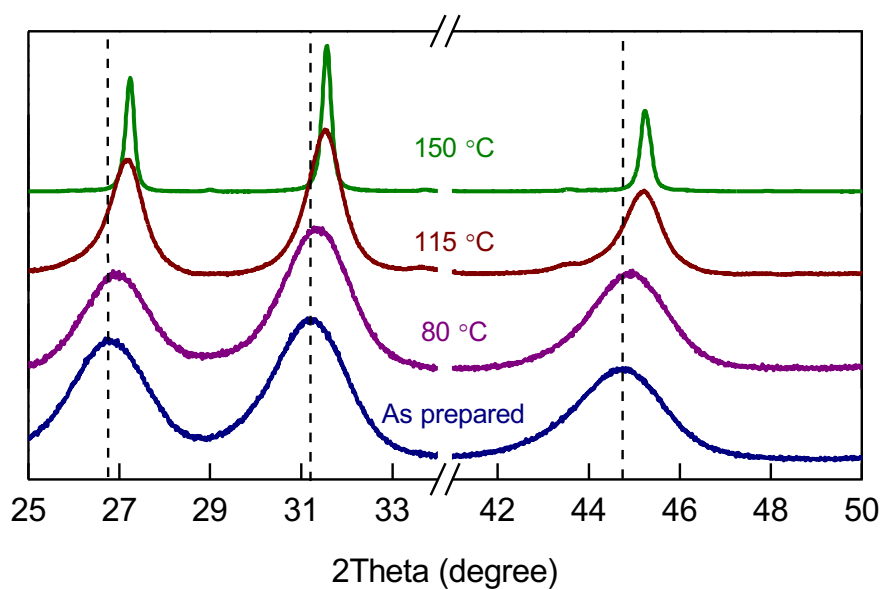
Figure S1 | Experimental X-ray diffraction patterns of AgBiS2 NC films annealed at different temperatures. X-ray diffraction patterns as-prepared (blue line), 80°C-annealed (magenta line), 115°C-annealed (wine line), and 150°C-annealed (green line) AgBiS$_2$ NC thin films. Dashlines are indications of peak positions before annealing. Clear and consistent peak shifts can be observed upon mild thermal annealing, confirming cation disorder homogenization, as demonstrated in Ref. [2].

Supporting Note 1: Analysis of Absorption Coefficients for AgBiS₂ NC Thin Films

As described in the Main Text, we interpret the absorption coefficients measured for our AgBiS₂ NC thin films through the bandgap fluctuation theory.[5] This theory was developed to describe absorption spectra in highly disordered systems and has been successfully used to describe the absorption coefficients in the near-bandgap region for a wide range of materials from kesterite to copper-indium semiconductors.[6,7]

On the other hand, several models have been developed to account for the effect of extensive disorder in the absorption spectra of semiconductor materials. For highly disordered materials, such as kesterites, it was demonstrated that a simple combination of the Urbach approach (i.e., assuming a simple exponential form of the absorption coefficient onset $\alpha \propto \exp(E/E_U)$, where E_u is the Urbach energy) and conventional square-root dependence of the density of states cannot fully account for the absorption spectrum [8]. A better description has been obtained with the bandgap fluctuation model, developed by Rau et al. [5,6]. Here, bandgap fluctuations occur as a result of disorder, causing a spatial variation of valence and conduction bands level. Following the statistical approach developed by Rau and co-workers [5,6], we assume a Gaussian distribution $G\big([E_{g,m}, \sigma_g]\big)$ of the bandgap E_g around an average bandgap $E_{g,m}$ with a width σ_g as follows:

$$G\big(E_g\big) = \frac{1}{\sigma_g \sqrt{2\pi}} \exp\left(-\frac{\big(E_g - E_{g,m}\big)^2}{\sigma_g^2} \right) \tag{S1}$$

Hence, the absorption coefficient can be expressed as

$$\alpha = \int\limits_0^\infty \alpha_0\big(E_g\big) \times G\big(E_g\big) \, dE_g, \tag{S2}$$

where α_0 is the absorption coefficient for a unique energy gap. In principle, this absorption coefficient α_0 depends on the band-structure of the material and Coulomb interactions, and can be expressed through a phenomenological model (e.g., Elliott model)[9].

However, in the case of AgBiS$_2$ NC films, we note that cryogenic measurements indicate the absence of strong Coulomb interaction in the material. Thus, by assuming the presence of a direct optically-allowed transition (as suggested by the absorption coefficient values $\alpha > 10^4 \text{cm}^{-1}$) and parabolic band dispersion, we can use $\alpha_0 = \frac{\sqrt{\hbar\omega - E_g}}{\hbar\omega}$ and obtain Eq. (1) reported in the Main Text. In Figure S2, we show the least-square fitting to the absorption coefficient of the studied AgBiS$_2$ NC films fabricated with a range of different thermal annealing procedures. We note that the bandgap fluctuation model provides a good description of the curves in the energy range of 0.7 - 1.8 eV. However, we observe that the model deviates from the experimental data at lower energies. As demonstrated by Crothers et al. [10], this effect is caused by unaccounted multiple reflections and the resulting optical interference effects in these ultra-thin films.

Obtained fitting parameters, shown in Figure 1c of the Main Text, reveal a correlated narrowing of the average energy gap and the distribution width. Overall, the Gaussian distribution width parameter is higher than what was previously reported for disordered materials such as kesterites $\sigma_g \approx$ 90 meV and for CIGS $\sigma_g \approx$ 65 meV [5,7]. Although cation disorder (e.g., segregation) is extensively present in our materials, we note that other factors could contribute to determining a broader absorption onset: (i) deviations from the parabolic band assumption including transitions between multiple bands; (ii) the effect of multiple reflections causing a broader absorption onset; (iii) choice of the fitting interval. Nevertheless, the obtained parameters reproduce well the effects and trends directly visible by inspecting the data shown in Figure 1a.
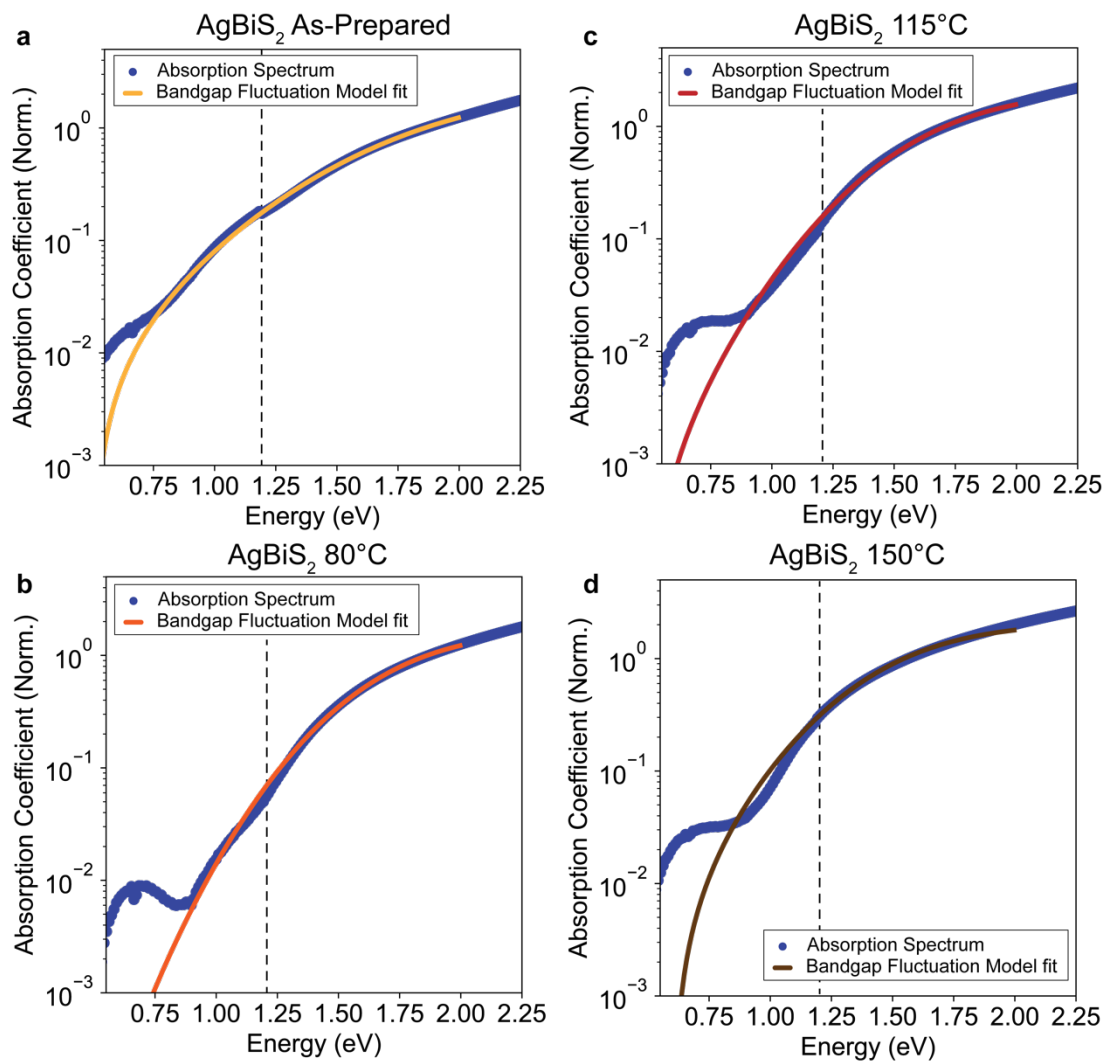
Figure S2 | Fits based on the bandgap fluctuation model to absorption coefficients for AgBiS₂ NC thin films.
Normalized absorption coefficients for (**a**) as-prepared, (**b**) 80°C-annealed, (**c**) 115°C-annealed, and (**d**) 150°C-annealed AgBiS₂ NC thin films. Blue dots represent experimental data, whereas fitting to the bandgap fluctuation model in the range 0.7-2 eV is reported as a solid line. Two absorption spectra - measured using InSb detector for energies below 1.22eV, and Si for energies above 1.22eV – are stitched to generate the reported experimental curves. Dashed lines indicate the detector change.

Supporting Note 2: Temperature-Dependent Bandgap Analysis

To determine and quantify the temperature dependence of the average bandgap extracted through the bandgap fluctuation model (see Supporting Note 1), we used the empirical Varshni model [11]. The Varshni equation defines the bandgap as a function of temperature as follows:

$$E_g(\text{T}) = \text{E}_{g,0} - \frac{\alpha T^2}{T + \beta} \tag{S3}$$

Here, α and β are fitting parameters characteristic of the material, and $\text{E}_{g,0}$ is the theoretical bandgap at 0 K. The resulting temperature dependence combines a quadratic low-temperature asymptotic behaviour and linear dependence at higher temperatures. Even though the theoretical basis for the Varshni fit is weak, building on a vague derivation of the parameters, it has been shown impirically to fit correctly the temperature-dependent bandgap for many group IV, II-VI, and III-V semiconductors [12], and has therefore become a useful approach to parametrize temperature trends in bandgaps.
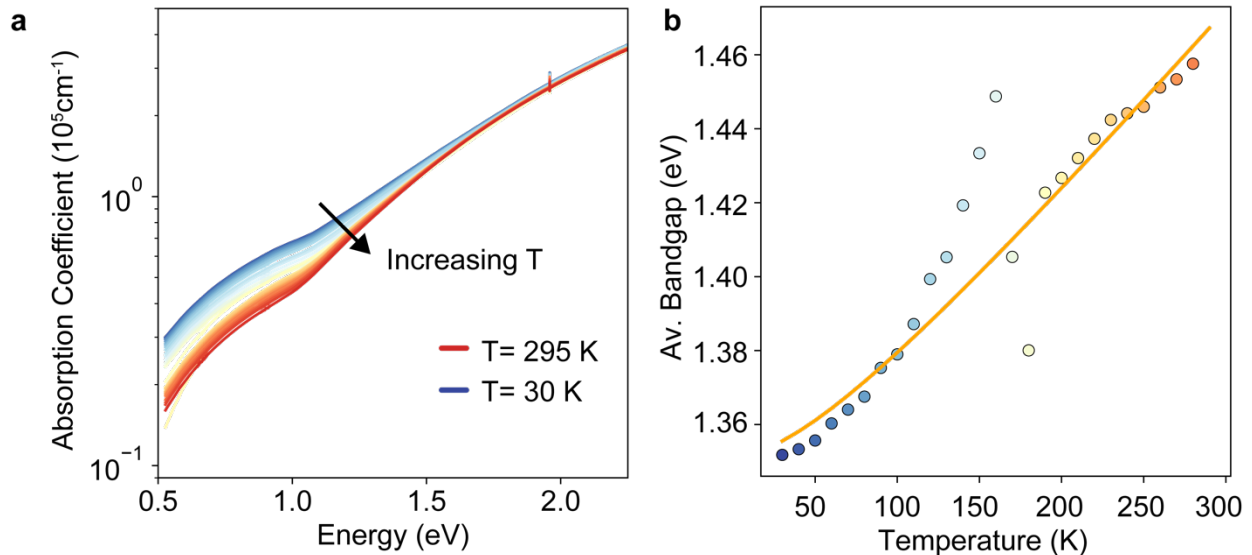

Figure S3 | Temperature-dependent absorption measurements for AgBiS$_2$ NC thin film annealed at 150°C.
(**a**) Temperature-dependent absorption coefficient for a AgBiS$_2$ NC thin film annealed at 150°C, measured between 30 K and 295 K. (**b**) Temperature dependence of the average band gap (E$_{g,m}$) for AgBiS$_2$ NC thin films annealed at 150°C. The orange line represents a fit to the Varshni model. Equivalent data and fits for the as-prepared (unannealed) AgBiS$_2$ NC thin film are shown in Figure 1 of the Main text.

Figure 1e in the Main Text and Figure S3b display the average bandgap (i.e. the bandgap extracted from fits based on the bandgap fluctuation model) together with Varshni fits based on Equation S3, for the as-prepared AgBiS$_2$ NC thin film and the film annealed at 150°C, respectively. The resulting values extracted for the fitting parameters α, β and E$_{g,0}$ are shown in Table S1 below:

Table S1: Parameters extracted from Varshni fits for the as-prepared AgBiS$_2$ NC thin film and the film annealed at 150°C .

	E$_{g,0}$ [eV]	α [meV/K]	β [K]
As-Prepared	1.50 ± 0.03	-1.2 ± 0.1	0 ± 20
150°C-Annealed	1.35 ± 0.04	-0.5 ± 0.2	83 ± 65

As described in the Main Text, a negative Varshni α parameter has been reported for many narrow and wide-bandgap semiconductors. This negative (or "inverse") Varshni behaviour has been a matter of intense debate, especially in the field of lead halide perovskites [13-15]. Two competing contributions generally determine the bandgap trends with temperature: (i) the temperature-dependent dilation of the lattice, affecting the energy bands; (ii) the temperature-dependent phonon population and the presence of different electron-phonon interactions [13]. Phonons in particular significantly affect the bandgap via the dynamic atomic displacement resulting from thermal lattice vibrations [16]. While phonons are usually considered to yield bandgap narrowing as the temperature is increased, the opposite effect and more complicated trend can be observed owing to the presence of multiple phonons with opposite contributions [17]. We further note that a discontinuity in the extracted average bandgap can be observed for both of the studied thin films at around 160 K (Figure 1e, and Figure S3b). The presence of

such discontinuities in both studied thin films could be indicative of a phase transition for AgBiS$_2$. However, further studies are needed to confirm this hypothesis.
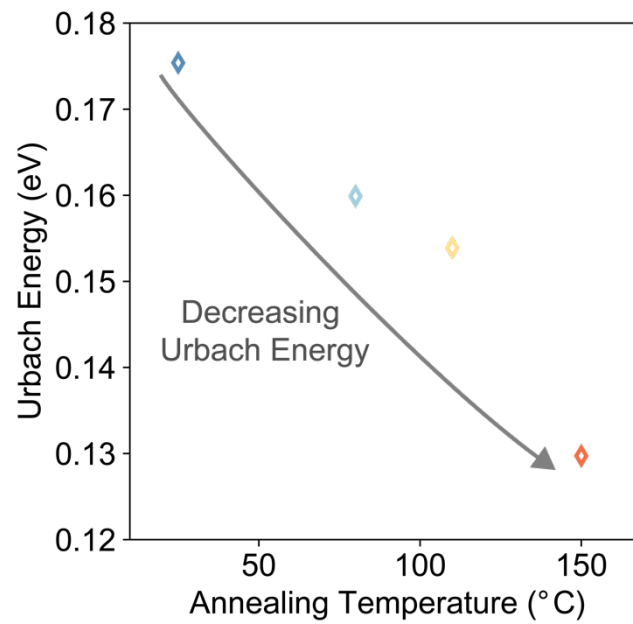

Figure S4 | Parameters extracted from fits based on the Urbach model. Urbach energies obtained by fitting the absorption edges of AgBiS$_2$ NC thin films to the Urbach model, plotted as a function of the film annealing temperature.
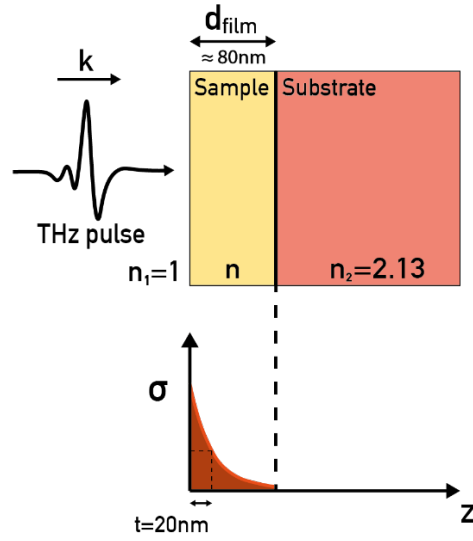
Figure S5 | Schematic illustration of sample geometry used in OPTP experiments. The AgBiS$_2$ NC thin film sample of thickness d_{film}~80nm is deposited on a 2-mm thick z-cut quartz substrate (n_2=2.13). Photoexcitation with a 400nm wavelength 35-fs laser pulse initially creates photoconductivity σ(z) with a Beer depth profile. Given the absorption coefficient (Figure 1b, Main Text) of the samples the 1/e-absorption depth *t* is approximately 20nm. The single cycle THz pulse probes the sample at normal incidence (i.e. z-direction) from vacuum (n_1=1). Note that the THz wavelength is much longer than the thickness of the sample thing film

Supporting Note 3: Derivation of charge-carrier mobility from OPTP

To determine the charge-carrier mobility from OPTP measurements, we followed the approach developed by Wehrenfennig et al. [18], and explained in detail by Xia et al. [19]. We converted the fractional change in THz transmission $\left(\frac{\Delta T}{T}\right)$ traces to a photoconductivity signal $\Delta\sigma$. This signal is proportional to the photoexcited charge carrier density *n* and to the charge-carrier mobility μ, as described by the relation $\Delta\sigma = en\mu$. As shown in Figure S5, given the high absorption coefficient α of the studied thin films (Figure 1b, Main Text), the photoexcited charge-carrier density *n* in our experiments varies significantly with the depth *z* as predicted by the Beer-Lambert law. The charge-carrier distribution resulting from photoexcitation therefore depends on the absorption coefficient α. We note that for film thicknesses $d_{film} < 1/\alpha$ the charge carrier distribution can be approximated as homogeneous in the thin film depth. On the

other hand, for film thicknesses $d_{film} > 1/\alpha$, the charge carrier can be approximated as concentrated in a "photoexcited layer" of thickness $1/\alpha$. As a result, the photoconductivity depends on the depth z as $\Delta\sigma(z) = \Delta\sigma_0 e^{-\alpha z}$, where $\Delta\sigma_0$ is the photoconductivity at the surface. In the configuration used in our measurements shown in Figure S5 (i.e., transmission geometry for thin films with high absorption coefficient on a z-cut quartz substrate), the photoconductivity can be approximated by

$$\Delta\sigma = -\frac{\epsilon_0 c(n_1 + n_3)}{t}\left(\frac{\Delta T}{T}\right), \qquad (S4)$$

where t is the thickness of the photoexcited layer $t = 1/\alpha$, and n_1 = 2.13 and n_3 = 1 are the refractive indexes of quartz and vacuum, respectively.[20]

The extraction of a value for the charge-carrier mobility does not require a knowledge of the depth profile of photoexcited charge carriers. As explained in detail previously by a range of groups [19,21,22], a solution to the wave equation in the geometry shown in Figure S5 and arbitrary conductivity profile $\Delta\sigma(z)$ gives

$$\Delta S = -\epsilon_0 c(n_1 + n_3)\left(\frac{\Delta T}{T}\right), \qquad (S5)$$

where,

$$\Delta S = \int_0^{d_{film}} \Delta\sigma(z)dz$$

is the sheet photoconductivity.

To quantify the charge-carrier mobility, the number of photogenerated charge carriers N must be determined. The number of photogenerated carriers is proportional to the number of absorbed photons, and is described as

$$N = \phi\frac{E\lambda}{hc}\left(1 - R_{pump} - T_{pump}\right), \qquad (S6)$$

where ϕ is the photon-to-charge branching ratio (i.e., the fraction of generated charges per photons absorbed), E is the excitation energy per pulse, and $\varepsilon = hc/\lambda$ is the energy of a photon with wavelength λ, and R and T are the sample transmittance and reflectance at the pump energy. The resulting effective mobility is:

$$\phi\mu = \frac{\Delta S \, A_{eff}}{N \, e} = -\epsilon_0 c(n_1 + n_3)\frac{A_{eff}hc}{eE\lambda(1 - R - T)}\left(\frac{\Delta T}{T}\right) \tag{S7}$$

Where A_{eff} is the effective area of overlap between the THz and the pump beam. As reported by Xia et al. [19], this is defined as $A_{eff} = 2\pi(\sigma_{pump}^2 + \sigma_{THz}^2)$, where σ_{pump} and σ_{THz} are the pump and THz beam waists, respectively. To avoid artifacts [23], in our experiments the ratio between σ_{pump} and σ_{THz} is fixed at ~6. Crucially, given the absence of excitonic interactions observed via temperature-dependent absorption spectra, we assume that $\phi\sim1$ and, therefore, the effective mobility to be reflective of the electron-hole sum mobility. Based on the two-level mobility model interpretation of our data (see Supporting Note 4 for further details), we extracted two different mobility values μ_i and μ_{loc}. Specifically, from the initial peak photoconductivity $\Delta\sigma(t = 1.5 \pm 0.5ps)$, we extracted μ_i by applying Equation S6 and S7, as shown by blue dots and lines in Figure S6. Furthermore, assuming the absence of charge-recombination processes during the initial ultrafast decay of the photoconductivity, we extracted by applying Equation S5 to the mobility after the localisation process $\Delta\sigma(t = 3 \pm 0.5ps)$, as shown by orange dots and lines in Figure S6.
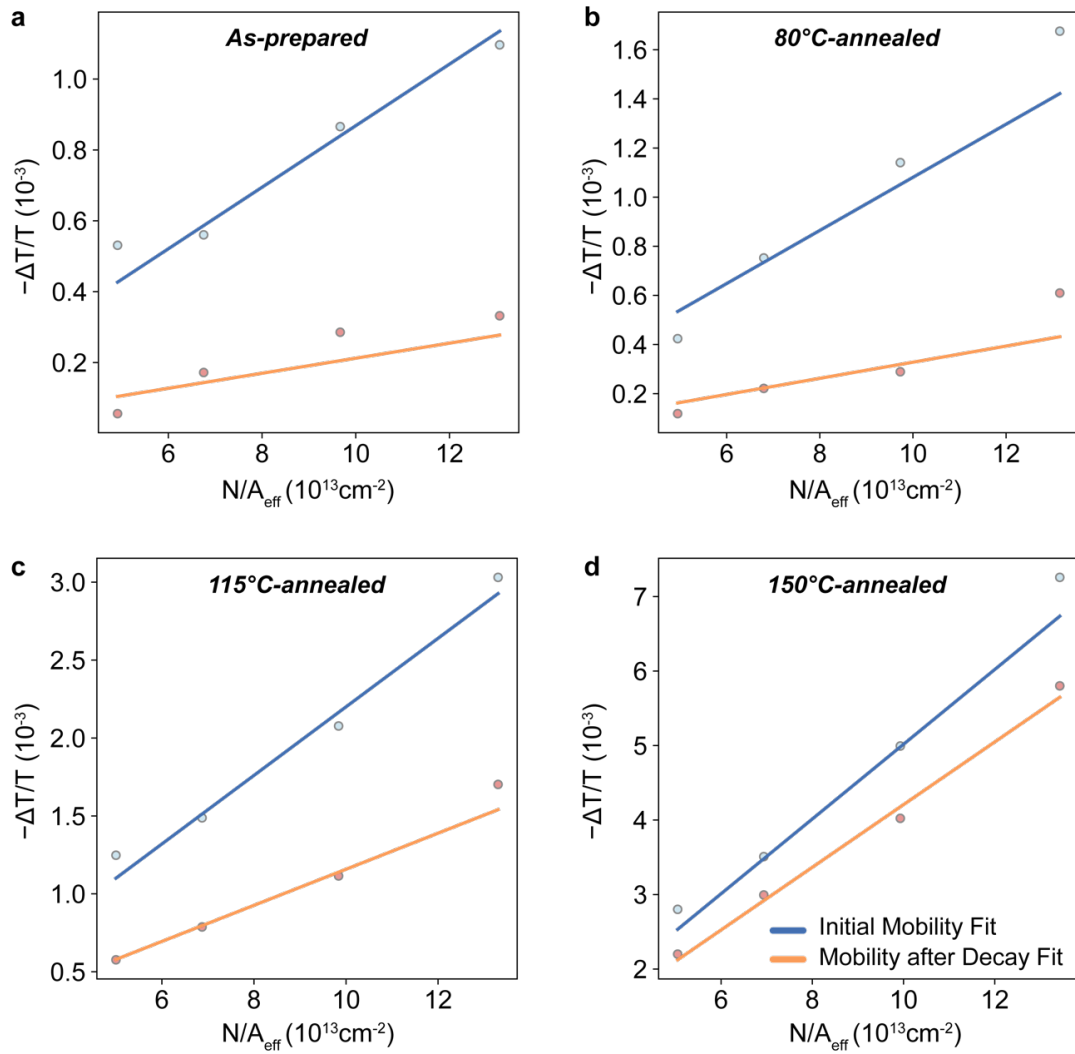
Figure S6 Determination of charge-carrier mobility for AgBiS$_2$ NC thin films. Fractional change in THz transmission amplitude $\Delta T/T$ following photoexcitation with a 3.1-eV pulsed laser, plotted as a function of the areal charge-carrier density for (**a**) as-prepared, (**b**) 80°C-annealed, (**c**) 115°C-annealed, and (**d**) 150°C-annealed AgBiS$_2$ NC thin films. Blue dots represent the initial maximum differential transmission of the THz electric field, $\Delta T/T$, following photoexcitation, and orange dots represent the $\Delta T/T$ values at 3 ps, after the ultrafast decay displayed in Figure S8. The lines shown are fits yielding a linear dependence on the areal charge-carrier density and allow to extraction of charge-carrier mobilities based on Eq. S5. Resulting mobilities are plotted in Figure 2e of the Main Text.

Supporting Note 4: Charge-Carrier Localisation in Silver-Bismuth Semiconductors and Two-Level Mobility Model

Charge-carrier localisation has been recently reported for a range of silver-bismuth and bismuth-based ABZ$_2$ semiconductors (e.g., Cs$_2$AgBiBr$_6$, Cu$_2$AgBiI$_6$, NaBiS$_2$,

15

Cu$_{4x}$(AgBi)$_{1-x}$I$_4$).[3,24-27] For these materials, THz photoconductivity transients have revealed an ultrafast decay of the initial photoconductivity signal, followed by a plateau with a long lifetime. Even though other processes (e.g., charge-carrier trapping, exciton formation, charge-carrier cooling) could yield a similar ultrafast decay, the fluence-independent behaviour of the observed signal and temperature-dependent OPTP experiments strongly supported the role of charge-carrier localisation. Crucially, temperature-dependent OPTP measurements on Cs$_2$AgBiBr$_6$ and Cu$_2$AgBiI$_6$ have revealed an opposite behaviour for the initial and the plateau OPTP signals. The initial OPTP signal has been observed to increase with lower temperatures, consistently with bandlike transport. On the other hand, the plateau OPTP signal has been shown to decrease with temperatures. [3,24-27] Crucially, such opposite temperature-dependent behaviour reflects a change in the transport regime, from bandlike to thermally-activated transport, following this ultrafast decay. We note that a similar temperature dependence of the OPTP signal is also observed for the AgBiS$_2$ NC thin film (Figure 3), thus suggesting that the observed ultrafast decay is caused by charge-carrier localisation.

To describe the presence of charge-carrier localization process in these materials, Wright et al. and Buizza et al. have proposed to fit the OPTP photoconductivity transients with a two-level mobility model.[3,24] In this model, the photoconductivity of the material originates from two different states with different populations and mobility: an initial delocalized state (n_i, μ_i) populated immediately after the photoexcitation and a localized state (n_{loc}, μ_{loc}) populated as a result of the charge-carrier localization process. The resulting sheet photoconductivity can be expressed as $\Delta S = \frac{e}{A_{eff}}(N_i\mu_i + N_{loc}\mu_{loc})$. By assuming a predominantly monomolecular charge-carrier recombination regime, as expected in the low fluence regime, we can describe the charge-carrier population of the two states by the following set of coupled rate equations:

16

$$\begin{cases} \dfrac{dN_i}{dt} = -k_{loc}N_i(t) \\ \dfrac{dN_{loc}}{dt} = k_{loc}N_i(t) - k_R N_{loc}(t) \end{cases} \tag{S8}$$

Here, k_{loc} and k_R are the charge-carrier localization and average recombination rates, respectively. The analytical solution to this set of differential equations yields the time-dependent charge carrier population for the two states. The resulting $\Delta T/T$ signal from combining Equation S7 and S8 is then:

$$\frac{\Delta T}{T} = -\frac{eN}{\epsilon_0 c(n_1 + n_3)A_{eff}}\left(\left(\mu_i - \frac{\mu_{loc}k_{loc}}{k_{loc} - k_R}\right)e^{-k_{loc}t} + \frac{\mu_{loc}k_{loc}}{k_{loc} - k_R}\,e^{-k_R t}\right) \tag{S9}$$

Furthermore, to account for the instrumental resolution and to fit the experimental data, we convoluted Eq. S9 with a Gaussian function with broadening $\sigma = 200\,fs$ (representing the instrumental response function) as described in Reference [3]. We used this model to fit room-temperature and low-temperature OPTP transients and thus demonstrate the presence of the charge-carrier localisation in AgBiS$_2$ NC films. On the other hand, we adopted a more robust method for extracting charge-carrier mobilities described in Supporting Note 3. We note that, for AgBiS$_2$ NC films and other silver-bismuth semiconductors studied so far, the mobility of the small polaron state has been observed to retain a non-negligible fraction of the initial large polaron mobility. Such behaviour may appear at odds with the large differences between mobilities reported for large and small polarons across a range of materials (>>1 cm^{2}V^{-1}s^{-1} and <1 cm^{2}V^{-1}s^{-1}, respectively) [28]. However, we also note that these values are generally derived from the comparison of materials that have significant differences in their physical and electronic structures. For instance, usually cited large polaron mobility values for GaAs and other III-V or II-VI semiconductors, are compared with those of small polarons in inorganic oxides and organic semiconductors. Crucially, however, these materials have radically

different band structures, and therefore often occupy vastly different mobility regimes. On the other hand, the ultrafast THz photoconductivity measurements of AgBiS$_2$ presented here reveal the difference between the transiently formed large polaron state and the final small polaron state within the same material. In addition, it is clear that the two concepts of "large" and "small" polarons are most valid for materials falling succinctly into either of the two extreme scenarios. However, ultimately a transition zone must exist, and this is where the recently explored bismuth halides and chalcogenides appear to fall, with mobilities of a few 1 cm^{2}V^{-1}s^{-1} that straddle the boundary. The AgBiS$_2$ material investigated here falls into this very regime of latent small polaronic effects, showing a transition from an initially large to a subsequently small polaron, that is strongly susceptible to the energetic landscape. Adequate theoretical models for such borderline systems do not exist to date – and are clearly a new challenge to materials modelling.

Photoconductivity Spectra

The frequency dependence of the photoconductivity signal gives further insight into the mechanism of charge-carrier transport. Different models have been used to describe these spectra and identify the contributing scattering mechanisms.[29] The Drude model describes the complex conductivity under an electric field oscillating with frequency ω, by assuming random scattering events with a characteristic scattering time τ that complete randomize the charge-carrier velocity.[30] The resulting Drude complex conductivity $\sigma_D(\omega)$ is:

$$\sigma_D(\omega) = \frac{ne^2\tau}{m^*}\left(\frac{1}{1 - i\omega\tau}\right) \tag{S10}$$

where n is the charge-carrier density, and m^* is the effective mass. Overall, this model accounts for the simple acceleration of charge carriers and the randomization of their momentum

randomized through scattering events with characteristic time τ between the events. To better describe the photoconductivity response of semiconductor nanomaterials, the Drude-Smith model has been introduced as a phenomenological adaptation of the Drude model, which includes directional scattering events (i.e., backscattering) to describe scattering from surfaces.[31] This phenomenological model was shown to be a special case within the formalism of memory functions [32]. Here, the backscattering event is described by the phenomenological c coefficient (varying from 0 to -1), where $c = -1$ indicates a complete velocity reversal on the first collision. According to the Drude-Smith formulation, the complex conductivity can be expressed as:

$$\sigma_{DS}(\omega) = \frac{ne^2\tau}{m^*}\left(\frac{1}{1-i\omega\tau} + \frac{c}{(1-i\omega\tau)^2}\right). \tag{S11}$$

Furthermore, in principle, the Drude-Smith model would allow the extraction of charge-carrier mobility value defined as $\mu_{DS} = (1 + c)\frac{e\tau}{m^*}$. However, we also note that in the limit of $c = -1$ μ_{DS} tends to infinity [33]. Therefore, in cases of substantial backscattering, μ_{DS} would be largely overestimated and its determination is avoided here.
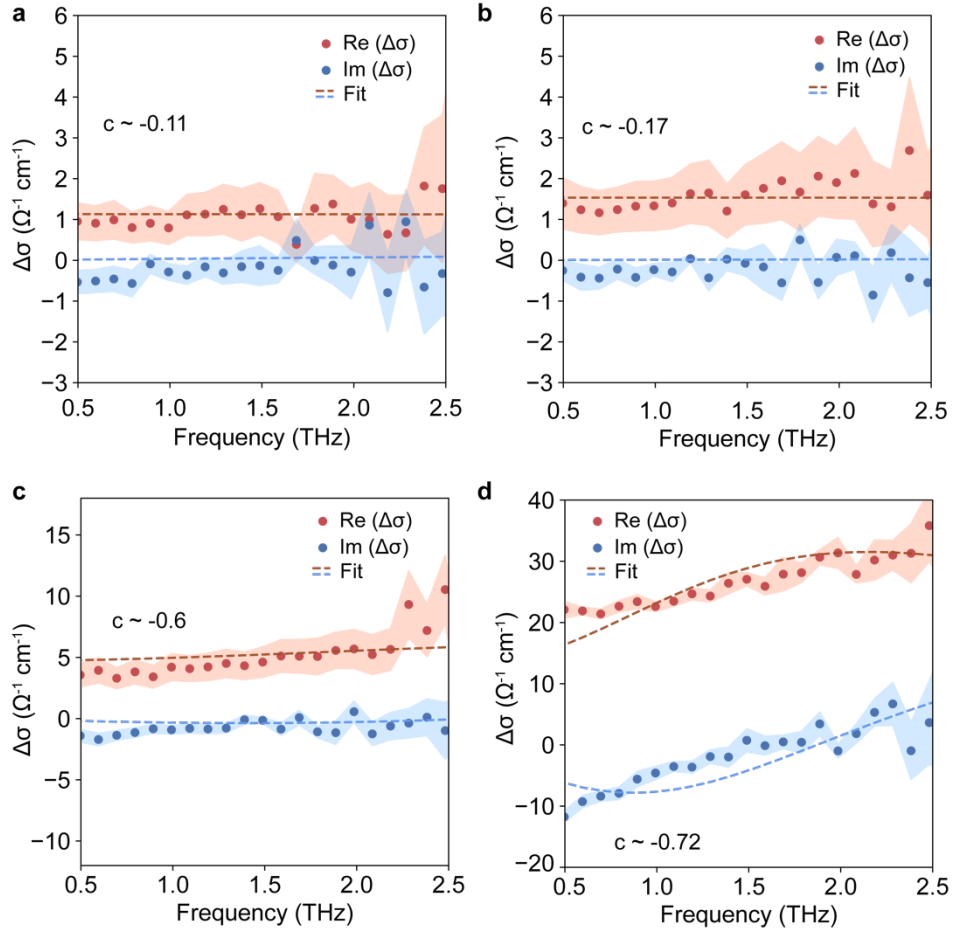
Figure S7 | Photoconductivity spectra for AgBiS₂ NC thin films. Terahertz photoconductivity spectra measured in the range 0.5-2.5 THz for (**a**) as-prepared, (**b**) 80°C-annealed, (**c**) 115°C-annealed, and (**d**) 150°C-annealed AgBiS$_2$ NC thin films. Spectra were measured in correspondence of the photoconductivity peak at a fluence of 78 µJ cm^{-2}. Red and blue dots represent the experimental data for the real and imaginary part of the photoconductivity, respectively. The shaded area indicates the standard deviation of the measured signal and give an estimate of the associated error. Dashed lines represent fitting to the Drude-Smith model (Equation S11), from which the extracted *c* parameters is calculated and reported for every fit in each corresponding panel.
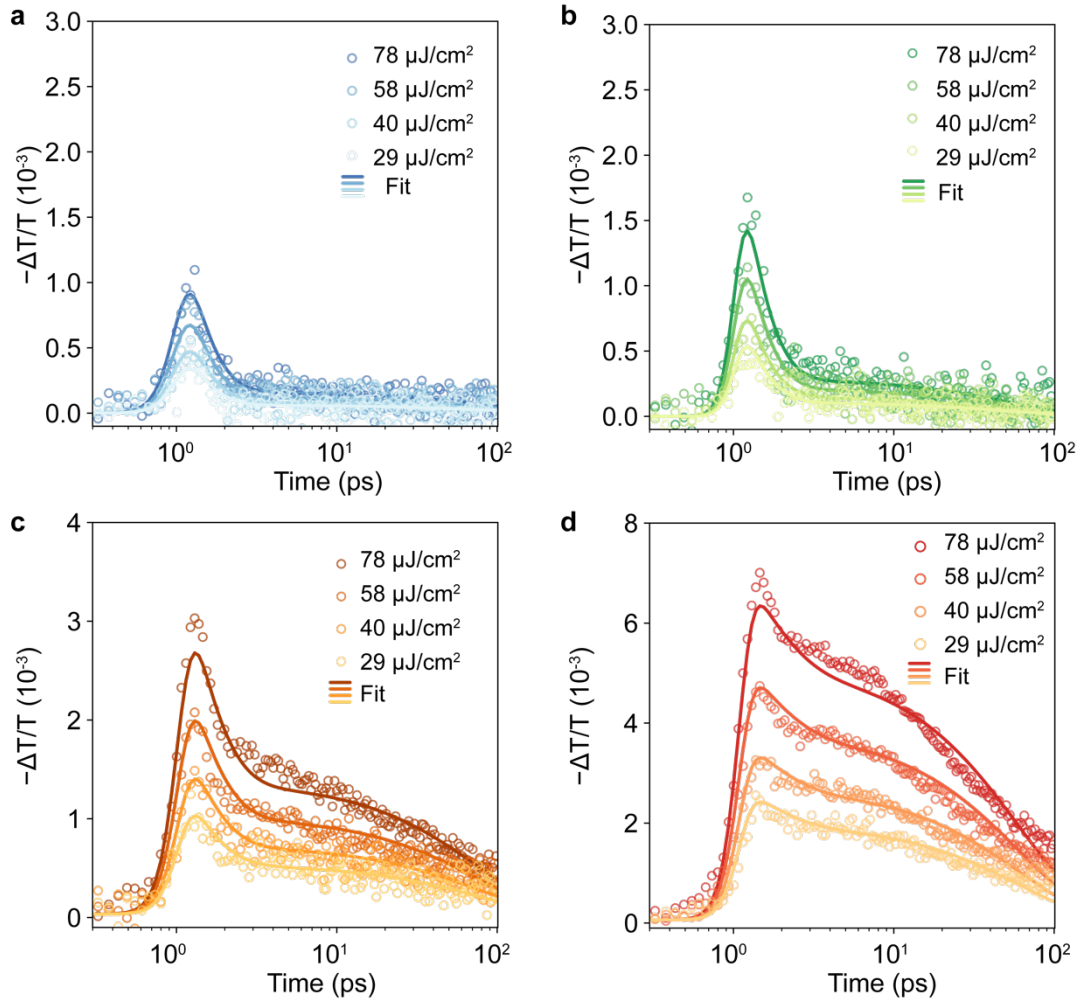
Figure S8 | Fluence-dependent OPTP measurements. Fluence-dependent OPTP transients measured for (**a**) as-prepared, (**b**) 80°C-annealed, (**c**) 115°C-annealed, and (**d**) 150°C-annealed AgBiS$_2$ NC thin films after 3.1-eV pulsed excitation. Solid lines represent fits to the two-level mobility model. Open circles are experimental data, and solid lines represent fits to the two-level mobility model.
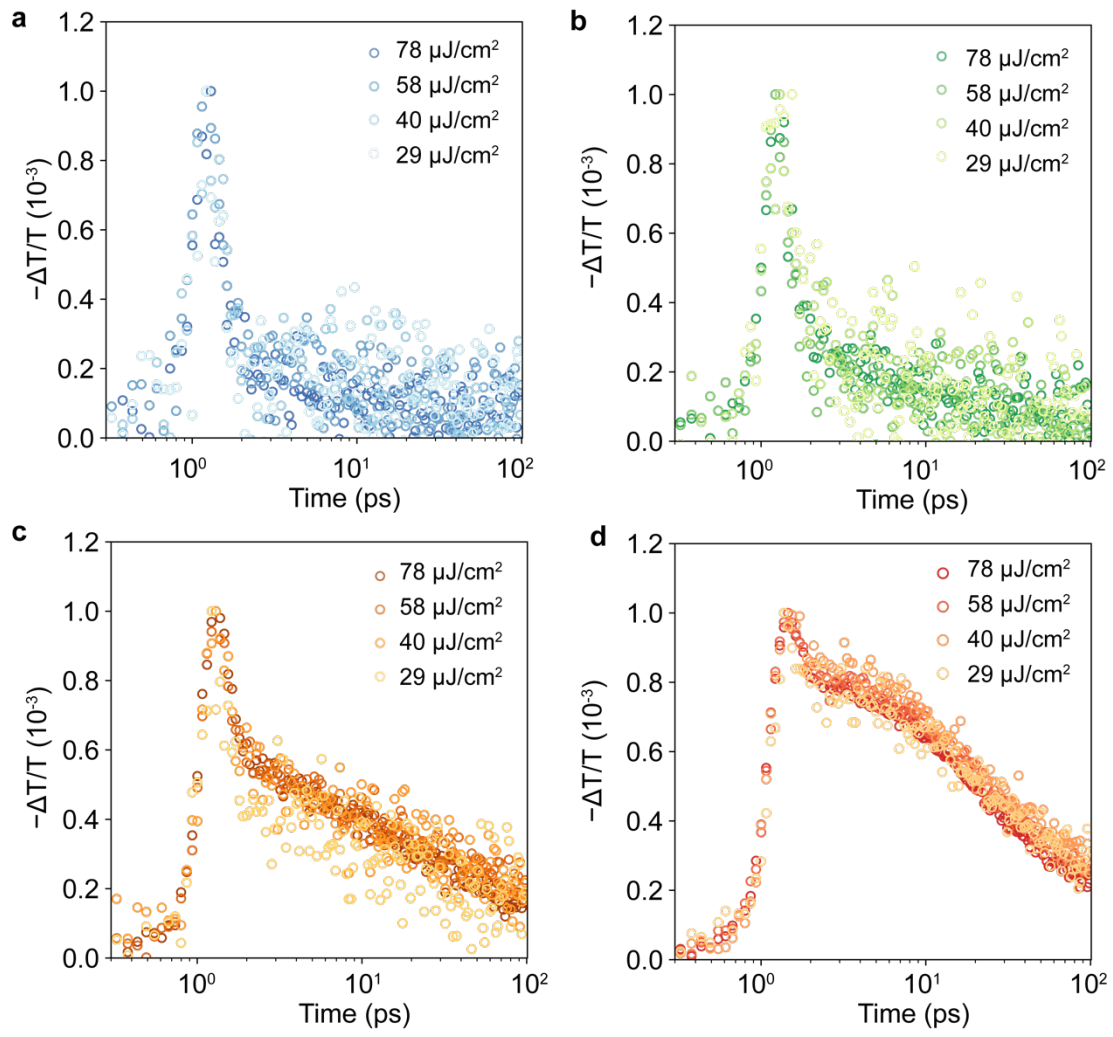
Figure S9 | Normalised Fluence-dependent OPTP measurements. Normalised comparison between fluence-dependent OPTP transients measured for (**a**) as-prepared, (**b**) 80°C-annealed, (**c**) 115°C-annealed, and (**d**) 150°C-annealed AgBiS$_2$ NC thin films after 3.1-eV pulsed excitation.
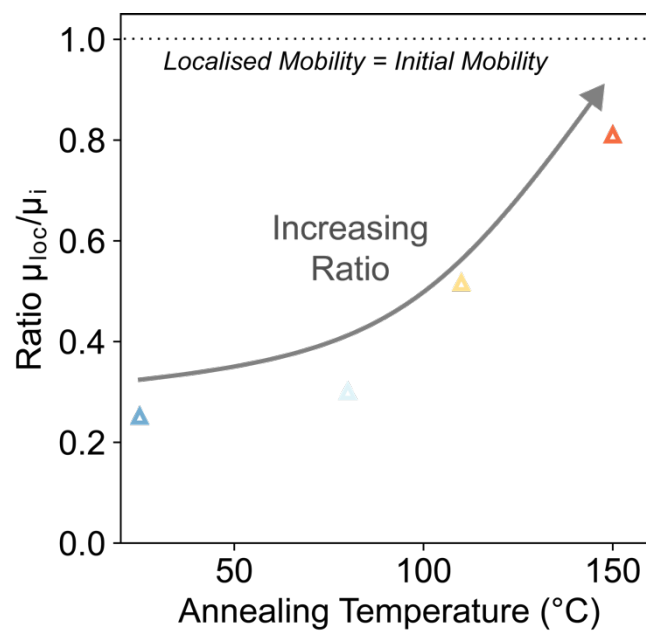
Figure S10 | Residual mobility ratio following ultrafast charge-carrier localization. Ratio between the localised and initial mobility for AgBiS$_2$ NC thin films annealing at different temperatures.

Supporting Note 5: Charge-Carrier Recombination Dynamics and Diffusion Lengths

Following the initial localisation process, well-described by the two-level mobility model, charge carriers undergo sub-nanosecond time scale recombination, as shown in Figure S8. Determining the charge-carrier recombination rate constants is of the utmost importance to extract charge-carrier diffusion lengths, in order to predict the performance of these materials in photovoltaic devices. The well-established k_1, k_2, k_3 (also known as ABC) model describes charge-carrier recombination dynamics in semiconductors as a combination of first (monomolecular), second (bimolecular), and third-order (Auger) recombination processes [34,35]. Given the fluence range (up to tens of μJ cm^{-2}) of our measurements, we limited the model to monomolecular and bimolecular recombination processes, and assumed negligible Auger contributions ($k_3 n^3 \sim 0$) to the observed recombinations. The resulting recombination dynamics is then described by the following rate equation:

$$\frac{dn}{dt} = -k_1 n - k_2 n^2, \tag{S12}$$

where n is the charge-carrier density, k_1 is the monomolecular recombination constant, which we ascribe to trap-mediated recombination processes, and k_2 is the bimolecular recombination constant, ascribed to the band-to-band radiative electron-hole recombination process.

To account for the spatial variation of n inside the measured thin films, we described the AgBiS$_2$ NC thin films as a series of slabs with different n. Here, we assumed an initial distribution according to the Beer-Lambert law $n(z) = n_0 e^{-(\alpha z)}$. In the fitting routine, charge-carrier recombination is determined by Equation S12 for each layer and summed to determine the charge-carrier recombination in the entire thin film. We globally fitted OPTP transients at different fluences to a numerical solution to this model via least-squares fitting. Fits are shown in Figure S11, and extracted parameters are reported in Table S2. We note that for as-prepared

AgBiS$_2$ NC thin films, the signal-to-noise ratio does not allow a reliable extraction of the parameters.

Table S2: Charge-carrier recombination rate constants for AgBiS$_2$ NC thin films. Values marked by * could not be obtained reliably because of the low signal-to-noise.

	k_1 [10^9 s^{-1}]	k_2 [10^{-10} cm^{-3} s^{-1}]
As-Prepared	(*)	(*)
80°C-Annealed	9.8	4.9
115°C-Annealed	2.9	4.4
150°C-Annealed	2.7	2.3

Finally, we combined the measured charge-carrier recombination rate constants and mobilities in order to estimate charge-carrier diffusion lengths for AgBiS$_2$ NC thin films, using the following equation:

$$L_D(n) = \sqrt{\frac{D}{R_{tot}(n)}} = \sqrt{\frac{\mu k_B T}{e R_{tot}(n)}} \tag{S13}$$

where R_{tot} is the total charge-carrier recombination rate, calculated as $R_{tot}(n) = k_1 + n k_2$. We note that, owing to the presence of bimolecular recombination processes, the charge-carrier diffusion length always depends on the charge-carrier density. In Table S3, we report the extracted charge-carrier diffusion lengths, for a charge-carrier density of 10^{16} cm^{-3}, for AgBiS$_2$ NC thin films and other selected reference materials. For materials undergoing charge-carrier localisation (including AgBiS$_2$ NC thin films), we considered only the diffusion of the localised state, assuming the contribution from the delocalised state to be negligible, given that it only

exists for at most a few picoseconds. We note that these diffusion length values are derived from THz photoconductivity measurements. This technique is sensitive to short-range, early-time charge-carrier mobility and thus mainly probes intra-NC crystal transport [33]. As such, the values we report here are thus reflective of the intrinsic semiconductor material quality and present an ideal scenario of conduction in the absence of boundary limitations. However, when NC boundaries present obstacles, our diffusion length calculations do not account for any ensuing long-range sub-diffusive transport regime, which may originate from dispersive processes such as inter-NC hopping, size distribution of the NCs, etc. A direct comparison between the value reported here and those derived from different techniques probing long-range conduction, such as space-charge-limited current, time-of-flight and photo-CELIV is thus complicated. In particular, we note that such dispersive, long-range transport will display lower charge-carrier mobilities, but also typically longer charge-carrier lifetimes [36]. Since the overall charge-carrier diffusion length depends on the product of both quantities, the drop in mobilities may therefore be counteracted by the increase in lifetimes. This feature can make direct comparison between long-range and short-range diffusion regimes difficult to compare, however, we note that the values we present here approximate the scenario of nano-crystal electrical connectivity with transport dominated by the intrinsic semiconductor properties.

In Figure 2f of the Main Text, we compare diffusion lengths estimated for $AgBiS_2$ NC thin films annealed at 150°C with other materials targeted for photovoltaic applications, based on data using the same experimental method of THz conductivity analysis. The diffusion lengths colourmap describes diffusion lengths in a 2D plot, calculated as described in Equation S13, as a function of charge-carrier mobility and lifetime (defined as $1/R_{tot}$); coloured triangles are the estimated diffusion lengths reported in Table S3.

Table S3: Charge-carrier recombination diffusion lengths for materials in this work, and selected materials from literature targeted as absorber layers in photovoltaic applications. References for the literature values are reported in the last column, * indicates this work.

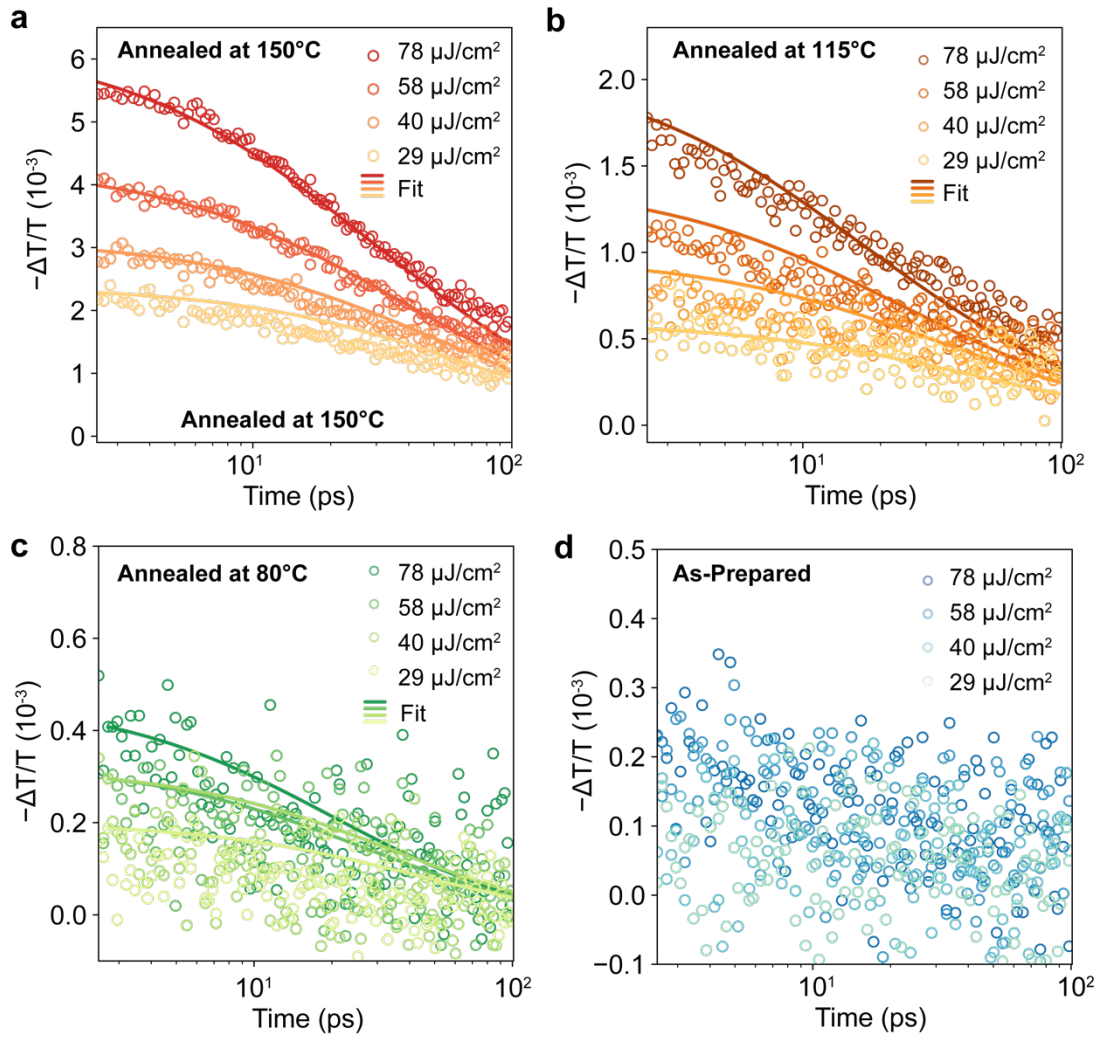|	μ [cm^2 V^{-1} s^{-1}]	k_1 [10^9 s^{-1}]	k_2 [10^{-9} cm^{-3} s^{-1}]	$R(n=10^{16}$cm^{-3}) [10^9 s^{-1}]	Diff. Length[nm]	Ref.
AgBiS$_2$ NCs 80°C	0.16	9.8	0.49	9.8	6	*
AgBiS$_2$ NCs 115°C	0.58	2.9	0.44	3.9	22	*
AgBiS$_2$ NCs 150°C	2.2	2.7	0.23	2.7	49	*
NaBiS$_2$	0.03	200	0	200	1	[27]
(FA,Cs)PbI$_3$	52	0.09	12	0.21	802	[37]
PbSe NCs	31	1.64	0	1.6	222	[38]
P3HT:PCBM	0.11	0.001	0.012	0.001	489	[39]
Cu$_2$AgBiI$_6$	1	0.2	2	0.22	109	[3]
Cs$_2$AgBiBr$_6$	1.3	3.3	0.045	3.2	32	[24]

Figure S11 | Fluence-dependent photoconductivity recombination dynamics, and global fits to the k_1k_2 model. Fluence-dependent charge-carrier recombination transients for (**a**) 150°C-annealed, (**b**) 115°C-annealed, (**c**) 80°C-annealed, and (**d**) as-prepared $AgBiS_2$ NC thin films. Experimental points were converted from measured photoconductivity transients, as described in Supporting Note 5. Solid lines represent fits to the recombination model described in Supporting Note 5. Obtained parameters are reported in Table S2.
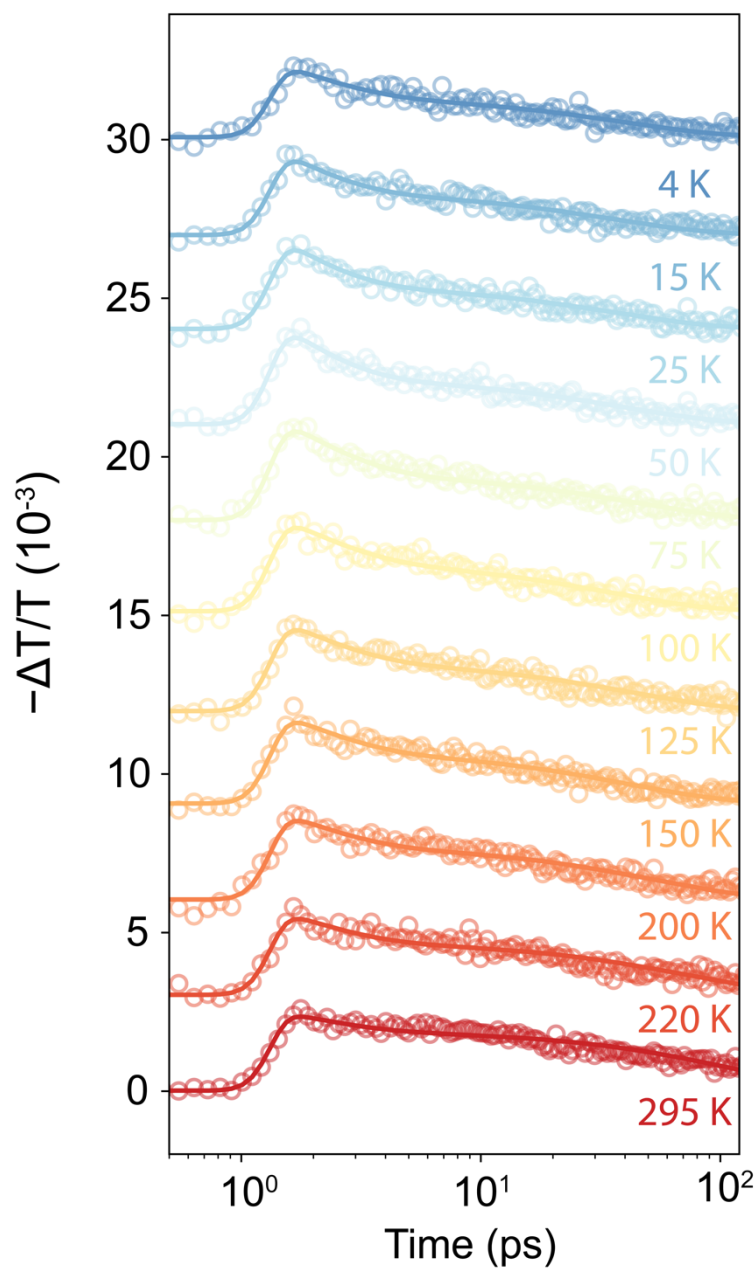
Figure S12 | Temperature-dependent OPTP transients. OPTP transients measured as a time after excitation for a range of different temperatures at an excitation fluence of 29 µJ cm^{-2}. Open circles represent experimental data, and coloured solid lines represent fits to the two-level mobility model. The two-level mobility model is explained schematically in Figure 3c of the Main Text, and the derivation of the model is explained in the Supporting Note 3. Charge-carrier localization and recombination rates extracted from these fits are shown in Figure S13.
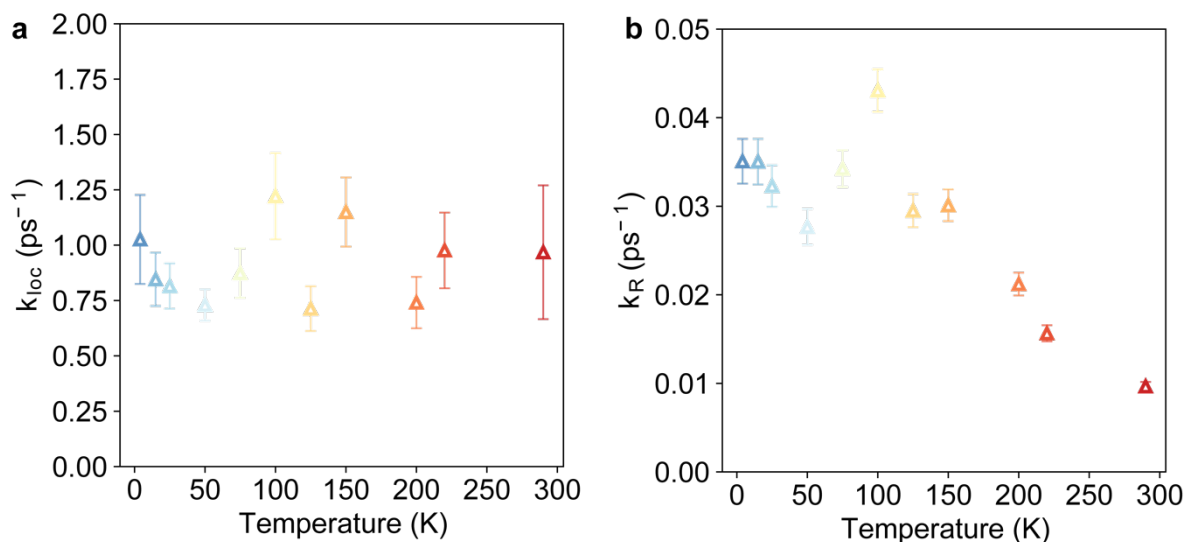
Figure S13 | Temperature-dependent localization and monomolecular recombination parameters. (**a**) Ultrafast localization rate and (**b**) recombination constant parameters obtained by fits of the two-level mobility model to temperature-dependent THz photoconductivity data, shown in Figure S12.

Temperature Dependence of Charge-Carrier Localisation in AgBiS$_2$ NC Thin Films

Temperature-Dependent Charge-Carrier Localisation and Recombination in AgBiS$_2$ NC Thin Films

Figure 3a compares the OPTP signal measured for 150°C-annealed AgBiS$_2$ NC thin film at room temperature and 4K. The two-level mobility model (described in Supplementary Note 4) describes well the observed dynamics for these two temperatures and the entire temperature-dependent OPTP dataset (Figure S12). The fitting parameters describing the dynamics (i.e., the localisation and recombination rates) are shown in Figure S13.

As shown in Figure S13a, we observe no significant temperature dependence in the localisation rate parameter. Therefore, we note that the more prominent localisation observed at 4K (Figure 3a) is caused by a more significant difference between the delocalised and localised mobility parameters.

As shown in Figure 3a of the Main Text, we also observe faster charge-carrier recombination at lower temperatures. The trend with temperature is well captured by the recombination constants extracted from fits to the two-level mobility model (Figure S13b). We note that in this model charge-carrier recombination is described by a general monoexponential decay term k_R. However, we have also shown that bimolecular recombination processes contribute to the charge-carrier recombination in this range of fluences (Figure 2d, Main Text). Therefore, k_R is expected to depend on the fluence and $1/k_R$ represents the time for the plateau photoconductivity to drop by $1/e$ lifetime at a fixed fluence, as a combination of monomolecular (trapping) and bimolecular (radiative) processes with the latter's dependence on charge-carrier density not captured here in this first-order approximation.

While we do not expect a significant increase in charge-carrier trapping rates at lower temperatures, we posit that this behavior originates from enhanced bimolecular recombination. A similar trend has been observed for more conventional semiconductors (e.g., GaAs) as well as lead halide perovskites, and has been attributed to the increased contribution from bimolecular recombination at lower temperatures [9,40]. The increased k_2 value for these materials has been shown to derive from the temperature-dependent thermal occupation of the electron−hole states near the band edge, therefore a narrowing of the Fermi-Dirac distribution at lower temperatures will lead to enhanced radiative electron-hole recombination rates.

Supporting References

(1)   Bernechea, M.; Cates, N.; Xercavins, G.; So, D.; Stavrinadis, A.; Konstantatos, G. Solution-processed solar cells based on environmentally friendly AgBiS$_2$ nanocrystals. *Nature Photonics* **2016**, *10*, 521-525.

(2)   Wang, Y.; Kavanagh, S. R.; Burgués-Ceballos, I.; Walsh, A.; Scanlon, D. O.; Konstantatos, G. Cation disorder engineering yields AgBiS$_2$ nanocrystals with enhanced optical absorption for efficient ultrathin solar cells. *Nature Photonics* **2022**, *16*, 235-241.

(3)   Buizza, L. R. V.; Wright, A. D.; Longo, G.; Sansom, H. C.; Xia, C. Q.; Rosseinsky, M. J.; Johnston, M. B.; Snaith, H. J.; Herz, L. M. Charge-Carrier Mobility and

Localization in Semiconducting Cu_2AgBiI_6 for Photovoltaic Applications. *ACS Energy Letters* **2021**, *6*, 1729-1739.

(4) Seifert, T.; Jaiswal, S.; Martens, U.; Hannegan, J.; Braun, L.; Maldonado, P.; Freimuth, F.; Kronenberg, A.; Henrizi, J.; Radu, I.; Beaurepaire, E.; Mokrousov, Y.; Oppeneer, P. M.; Jourdan, M.; Jakob, G.; Turchinovich, D.; Hayden, L. M.; Wolf, M.; Münzenberg, M.; Kläui, M.; Kampfrath, T. Efficient metallic spintronic emitters of ultrabroadband terahertz radiation. *Nature Photonics* **2016**, *10*, 483-488.

(5) Rau, U.; Werner, J. H. Radiative efficiency limits of solar cells with lateral band-gap fluctuations. *Applied Physics Letters* **2004**, *84*, 3735-3737.

(6) Mattheis, J.; Rau, U.; Werner, J. H. Light absorption and emission in semiconductors with band gap fluctuations—A study on $Cu(In,Ga)Se_2$ thin films. *Journal of Applied Physics* **2007**, *101*, 113519.

(7) Gokmen, T.; Gunawan, O.; Todorov, T. K.; Mitzi, D. B. Band tailing and efficiency limitation in kesterite solar cells. *Applied Physics Letters* **2013**, *103*, 103506.

(8) Rey, G.; Larramona, G.; Bourdais, S.; Choné, C.; Delatouche, B.; Jacob, A.; Dennler, G.; Siebentritt, S. On the origin of band-tails in kesterite. *Solar Energy Materials and Solar Cells* **2018**, *179*, 142-151.

(9) Davies, C. L.; Filip, M. R.; Patel, J. B.; Crothers, T. W.; Verdi, C.; Wright, A. D.; Milot, R. L.; Giustino, F.; Johnston, M. B.; Herz, L. M. Bimolecular recombination in methylammonium lead triiodide perovskite is an inverse absorption process. *Nature Communications* **2018**, *9*, 293.

(10) Crothers, T. W.; Milot, R. L.; Patel, J. B.; Parrott, E. S.; Schlipf, J.; Müller-Buschbaum, P.; Johnston, M. B.; Herz, L. M. Photon Reabsorption Masks Intrinsic Bimolecular Charge-Carrier Recombination in $CH_3NH_3PbI_3$ Perovskite. *Nano Letters* **2017**, *17*, 5782-5789.

(11) Varshni, Y. P. Temperature dependence of the energy gap in semiconductors. *Physica* **1967**, *34*, 149-154.

(12) Sarswat, P. K.; Free, M. L. A study of energy band gap versus temperature for Cu_2ZnSnS_4 thin films. *Physica B: Condensed Matter* **2012**, *407*, 108-111.

(13) Parrott, E. S.; Green, T.; Milot, R. L.; Johnston, M. B.; Snaith, H. J.; Herz, L. M. Interplay of Structural and Optoelectronic Properties in Formamidinium Mixed Tin–Lead Triiodide Perovskites. *Advanced Functional Materials* **2018**, *28*, 1802803.

(14) Whalley, L. D.; Skelton, J. M.; Frost, J. M.; Walsh, A. Phonon anharmonicity, lifetimes, and thermal transport in $CH_3NH_3PbI_3$ from many-body perturbation theory. *Physical Review B* **2016**, *94*, 220301.

(15) Kim, H.; Hunger, J.; Cánovas, E.; Karakus, M.; Mics, Z.; Grechko, M.; Turchinovich, D.; Parekh, S. H.; Bonn, M. Direct observation of mode-specific phonon-band gap coupling in methylammonium lead halide perovskites. *Nature Communications* **2017**, *8*, 687.

(16) Fan, H. Y. Temperature Dependence of the Energy Gap in Semiconductors. *Physical Review* **1951**, *82*, 900-905.

(17) Göbel, A.; Ruf, T.; Cardona, M.; Lin, C. T.; Wrzesinski, J.; Steube, M.; Reimann, K.; Merle, J. C.; Joucla, M. Effects of the isotopic composition on the fundamental gap of CuCl. *Physical Review B* **1998**, *57*, 15183-15190.

(18) Wehrenfennig, C.; Eperon, G. E.; Johnston, M. B.; Snaith, H. J.; Herz, L. M. High Charge Carrier Mobilities and Lifetimes in Organolead Trihalide Perovskites. *Advanced Materials* **2014**, *26*, 1584-1589.

(19) Xia, C. Q.; Peng, J.; Poncé, S.; Patel, J. B.; Wright, A. D.; Crothers, T. W.; Uller Rothmann, M.; Borchert, J.; Milot, R. L.; Kraus, H.; Lin, Q.; Giustino, F.; Herz, L. M.;

Johnston, M. B. Limits to Electrical Mobility in Lead-Halide Perovskite Semiconductors. *The Journal of Physical Chemistry Letters* **2021**, *12*, 3607-3617.

(20) Joyce, H. J.; Boland, J. L.; Davies, C. L.; Baig, S. A.; Johnston, M. B. A review of the electrical properties of semiconductor nanowires: insights gained from terahertz conductivity spectroscopy. *Semiconductor Science and Technology* **2016**, *31*, 103003.

(21) D'Angelo, F.; Němec, H.; Parekh, S. H.; Kužel, P.; Bonn, M.; Turchinovich, D. Self-referenced ultra-broadband transient terahertz spectroscopy using air-photonics. *Opt. Express* **2016**, *24*, 10157-10171.

(22) Kužel, P.; Němec, H. Terahertz conductivity in nanoscaled systems: effective medium theory aspects. *Journal of Physics D: Applied Physics* **2014**, *47*, 374005.

(23) Beard, M. C.; Turner, G. M.; Schmuttenmaer, C. A. Transient photoconductivity in GaAs as measured by time-resolved terahertz spectroscopy. *Physical Review B* **2000**, *62*, 15764-15777.

(24) Wright, A. D.; Buizza, L. R. V.; Savill, K. J.; Longo, G.; Snaith, H. J.; Johnston, M. B.; Herz, L. M. Ultrafast Excited-State Localization in $Cs_2AgBiBr_6$ Double Perovskite. *The Journal of Physical Chemistry Letters* **2021**, *12*, 3352-3360.

(25) Buizza, L. R. V.; Sansom, H. C.; Wright, A. D.; Ulatowski, A. M.; Johnston, M. B.; Snaith, H. J.; Herz, L. M. Interplay of Structure, Charge-Carrier Localization and Dynamics in Copper-Silver-Bismuth-Halide Semiconductors. *Advanced Functional Materials* **2022**, *32*, 2108392.

(26) Wu, B.; Ning, W.; Xu, Q.; Manjappa, M.; Feng, M.; Ye, S.; Fu, J.; Lie, S.; Yin, T.; Wang, F.; Goh, T. W.; Harikesh, P. C.; Tay, Y. K. E.; Shen, Z. X.; Huang, F.; Singh, R.; Zhou, G.; Gao, F.; Sum, T. C. Strong self-trapping by deformation potential limits photovoltaic performance in bismuth double perovskite. *Science Advances*, *7*, eabd3160.

(27) Huang, Y.-T.; Kavanagh, S. R.; Righetto, M.; Rusu, M.; Levine, I.; Unold, T.; Zelewski, S. J.; Sneyd, A. J.; Zhang, K.; Dai, L.; Britton, A. J.; Ye, J.; Julin, J.; Napari, M.; Zhang, Z.; Xiao, J.; Laitinen, M.; Torrente-Murciano, L.; Stranks, S. D.; Rao, A.; Herz, L. M.; Scanlon, D. O.; Walsh, A.; Hoye, R. L. Z. Strong absorption and ultrafast localisation in $NaBiS_2$ nanocrystals with slow charge-carrier recombination. *Nature Communications* **2022**, *13*, 4960.

(28) Franchini, C.; Reticcioli, M.; Setvin, M.; Diebold, U. Polarons in materials. *Nature Reviews Materials* **2021**, *6*, 560-586.

(29) Ulatowski, A. M.; Herz, L. M.; Johnston, M. B. Terahertz Conductivity Analysis for Highly Doped Thin-Film Semiconductors. *Journal of Infrared, Millimeter, and Terahertz Waves* **2020**, *41*, 1431-1449.

(30) Herz, L. M. Charge-Carrier Mobilities in Metal Halide Perovskites: Fundamental Mechanisms and Limits. *ACS Energy Letters* **2017**, *2*, 1539-1548.

(31) La-o-vorakiat, C.; Salim, T.; Kadro, J.; Khuc, M.-T.; Haselsberger, R.; Cheng, L.; Xia, H.; Gurzadyan, G. G.; Su, H.; Lam, Y. M.; Marcus, R. A.; Michel-Beyerle, M.-E.; Chia, E. E. M. Elucidating the role of disorder and free-carrier recombination kinetics in CH3NH3PbI3 perovskite films. *Nature Communications* **2015**, *6*, 7903.

(32) Chen, W.-C.; Marcus, R. A. The Drude-Smith Equation and Related Equations for the Frequency-Dependent Electrical Conductivity of Materials: Insight from a Memory Function Formalism. *ChemPhysChem* **2021**, *22*, 1667-1674.

(33) Motti, S. G.; Krieg, F.; Ramadan, A. J.; Patel, J. B.; Snaith, H. J.; Kovalenko, M. V.; Johnston, M. B.; Herz, L. M. CsPbBr3 Nanocrystal Films: Deviations from Bulk Vibrational and Optoelectronic Properties. *Advanced Functional Materials* **2020**, *30*, 1909904.

(34) Herz, L. M. Charge-Carrier Dynamics in Organic-Inorganic Metal Halide Perovskites. *Annual Review of Physical Chemistry* **2016**, *67*, 65-89.

(35)   Sum, T. C.; Righetto, M.; Lim, S. S. Quo vadis, perovskite emitters? *The Journal of Chemical Physics* **2020**, *152*, 130901.

(36)   Wright, A. D.; Milot, R. L.; Eperon, G. E.; Snaith, H. J.; Johnston, M. B.; Herz, L. M. Band-Tail Recombination in Hybrid Lead Iodide Perovskite. *Advanced Functional Materials* **2017**, *27*, 1700860.

(37)   Lohmann, K. B.; Motti, S. G.; Oliver, R. D. J.; Ramadan, A. J.; Sansom, H. C.; Yuan, Q.; Elmestekawy, K. A.; Patel, J. B.; Ball, J. M.; Herz, L. M.; Snaith, H. J.; Johnston, M. B. Solvent-Free Method for Defect Reduction and Improved Performance of p-i-n Vapor-Deposited Perovskite Solar Cells. *ACS Energy Letters* **2022**, *7*, 1903-1911.

(38)   Guglietta, G. W.; Diroll, B. T.; Gaulding, E. A.; Fordham, J. L.; Li, S.; Murray, C. B.; Baxter, J. B. Lifetime, Mobility, and Diffusion of Photoexcited Carriers in Ligand-Exchanged Lead Selenide Nanocrystal Films Measured by Time-Resolved Terahertz Spectroscopy. *ACS Nano* **2015**, *9*, 1820-1828.

(39)   Parkinson, P.; Lloyd-Hughes, J.; Johnston, M. B.; Herz, L. M. Efficient generation of charges via below-gap photoexcitation of polymer-fullerene blend films investigated by terahertz spectroscopy. *Physical Review B* **2008**, *78*, 115321.

(40)   t Hooft, G. W.; Leys, M. R.; Talen-v.d. Mheen, H. J. Temperature dependence of the radiative recombination coefficient in GaAs   (Al, Ga)As quantum wells. *Superlattices and Microstructures* **1985**, *1*, 307-310.